Semi-automatic detection of buried rebar in GPR data using a genetic algorithm☆

Yanhui Wang[a,b,c,d], Guangyan Cui[a,b,c,*], Jun Xu[e]

[a] *State Key Laboratory of Rail Traffic Control and Safety, Beijing Jiaotong University, Beijing 100044, China*
[b] *School of traffic and transportation, Beijing Jiaotong University, Beijing 100044, China*
[c] *Research and Development Center of Transport Industry of Technologies and Equipment of Urban Rail Operation Safety Management, Beijing 100044, China*
[d] *Beijing Research Center of Urban Traffic Information Sensing and Service Technology, Beijing Jiaotong University, Beijing 100044, China*
[e] *Department of Civil Engineering, University of Science & Technology Beijing, Beijing 100083, China*

ARTICLE INFO

ABSTRACT

This paper proposes a new method for semi-automatic detection of buried rebar in ground penetrating radar (GPR) data based on searching the reflected waveform of target by the genetic algorithm, which aims to overcome the inefficiency and instability of the manual process. Before the detection step, a binary image is generated by collecting all the local maximum points from A-scan GPR data to turn the searching for waveform image into curves. Meanwhile, the possible locations of the targets are preliminarily selected from the gray-scale frequency-wavenumber domain migration image of GPR data by setting a gray gradient threshold in the vertical direction. Then based on the genetic algorithm and time-distance analysis of the reflected signal, semi-automatic detection could be achieved by searching the best fitting hyperbola at every potential location in the binary image, and matching them with the reflected signal of targets according to several carefully chosen matching criteria. The impact of waveform distortion is also considered in the matching process to ensure a good adaptability of this method to the GPR data. Precision and efficiency of this method are analyzed lastly by four measured data of different antenna frequencies and targets, the average misjudgment and the undetected rate are 9.08% and 11.98% respectively. Meanwhile, the same GPR data is detected by four antenna central frequencies to find that the missed rate of semi-automatic detection decreases with the increase of the antenna frequency, when the misjudgment rate remains stable.

1. Introduction

Ground Penetrating Radar (GPR) is a non-destructive method that images the subsurface and detects the underground medium distribution with ultra-high frequency pulsed electromagnetic waves [1,2], which has been widely applied in many fields like geological exploration [3,4], archeology [5,6], quality testing in civil engineering [7–10] and road inspection [11,12] due to its fast, convenient and high resolution features [13,14].

For the buried target with different kinds of permittivity, electromagnetic waves will reflect or refract along with the target interfaces during transmission, so the buried target could be defined according to the variation of return signal. Meanwhile, the position, buried depth, and structure of the targets could also be defined [15]. However, in most field GPR detections, there is often a large amount of noise generated along with the reflected waves of the target from the site

disturbance (such as inhomogeneous medium, large equipment nearby, etc.), causing the GPR image interpretation to be more complicated and difficult [16]. Besides, the reflected waves of the target will be distorted or partially missed due to the non-ideal situation in the collecting process, leading to more labor-intensive and time-consuming of the manual detection. Furthermore, the accuracy of the collected GPR profiles are determined and recognized by the experience of the operators.

In view of the shortcomings of the manual process, the automatic detection method has long been a hotspot in the GPR application area. Qader et al. [17] presented a framework for the automatic detection and localization of defects inside bridge decks based on feature extraction algorithm and banded-independent component analysis. Pasolli et al. [18] proposed a novel pattern recognition system by using the Genetic Algorithm (GA) to identify buried objects in Finite-Difference Time-Domain (FDTD) data. Al-Nuaimy et al. [19] acquired the
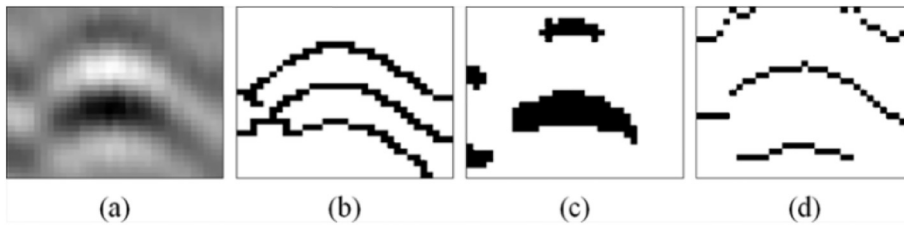
Fig. 1. Edge detection results of the same GPR image by different algorithms: (a) gray-scale GPR image, (b) edge detected by Canny filter, (c) edge detected by Kapur binarization, and (d) edge detected by collecting the local maximum values in every A-scan data.

automatic positioning of buried utilities by neural network training and pattern recognition method. Besaw et al. [20] achieved in the field of object classification by using the Cellular Neural Network (CNN) method and the signatures of 2-dimensional GPR data are also extracted. Many other advanced processes based on mathematical methods [21,22], image or signal processing methods such as Hough [23,24], wavelet [25,26] transforms, or image recognition methods [27,28] have also been developed by worldwide researchers.

The existing processes mainly consist of two steps. First, the matching model is established by combining meaningful features of the target echo (amplitude, frequency situation, hyperbola edge, etc.) or by Machine Learning (ML) method [29,30], Neural Network [31] and Deep Belief Network [32]. Wentai Lei et al. [33] proposed a method called trained deep learning framework to identify the hyperbolic signatures of targets at the beginning of automatic detection. To overcome the time-consuming and labor-intensive in the rebar detection in the engineering, Kien Dinh et al. [34] integrate the two methods of Cellular Neural Network and image processed. And then they searched for regions or points by using the matching model. However, both the efficiency and precision were greatly affected in many cases as the process was executed in a field GPR data with various noises.

Although these methods have been widely used in the GPR non-destructive testing and made many breakthrough achievements recently, which are also equally controversial and deficient to some extent. The ML methods can narrow down the search intervals, however, which are limited by the amount of the processing GPR data. The CNN methods achieved a rapid development for the hyperbola detection in recent years. Nevertheless, the lacking in the target extracting and the limit of size of the input on-site GPR images both hinder the further development [33]. The genetic algorithm proposed in our paper can detect hyperbolic edge of targets, and then extract the hyperbola that best matches the search model in the sub-window.

This paper aims to present a semi-automatic method for the detection of buried targets in GPR data based on the hyperbolic edge detected. The method comprises data preprocessing and target detection stages. Firstly, GPR data is screened in the preprocessing stage, including converting the gray-scale GPR image into a binary image and selecting the potential positions of targets. The converting step is achieved by transforming all the local maximum points of every A-scan GPR data into a binary image, then converting the search of specific echo waveform images into the search of hyperbolic edges in binary images. This will be more efficient and precise in the detection of buried rebar next. The selection of the potential positions is a simulation of the manual detection process, which can greatly narrow the search of targets. This step is achieved by selecting the positions in the Frequency-Wavenumber domain (FK) migration image of GPR data, according to the value of the comparison in the vertical gray gradient. In the target detection stage, firstly several rectangular sub-windows centered on each potential position are isolated from the binary image, with their size automatically calculated by the antenna center frequency and two-way travel time of the potential position. Afterward, GA is applied in the next step to search for the fitting hyperbola that obeys the time-distance relationship and covers the most edge pixels in every sub-window. Semi-automatic detection could be achieved by searching the best fitting hyperbola at every potential location in the binary image, and matching them with the reflected signal of targets

according to several carefully chosen matching criteria. This method is tested by eight measured GPR data with different antenna central frequencies, and the precision as well as the efficiency are validated in comparison with the results of the manual process.

The rest of this paper is organized as follows. The data preprocessing of the method proposed in this paper, including Edge Detection and Selection of Potential Positions, is presented in Section 2. The sub-window and time-distance relationship are proposed in Section 3, and the experimental precision is analyzed and compared with the manual results in Section 4. Finally, the conclusions are summarized in Section 5.

2. Data preprocessing

2.1. Edge detection

The semi-automatic detection of targets can be achieved by searching the GPR B-scan image for specific electromagnetic waveforms reflecting from the targets. While automatically searching the waveforms in a GPR image directly by the image detection algorithm, it is usually difficult to get an expected detection precision [35–37], as the reflecting signals of different targets differ in many ways. A better solution is to transform the gray-scale GPR image into a binary image by edge detection operation or binarization method. As for a discontinuous target, the return signal can be described by hyperbolic equation approximately. Thus, to carry out the detection of buried targets, it only needs to find out all hyperbolic edges in the binary image, which is more easily and quickly compared with the image detection process.

The Canny filter [38] and the Kapur binarization are commonly used in the edge detection of the GPR image. As shown in Fig. 1, edges detected from the same GPR data vary according to different algorithms. [Fig. 1(a)] shows the gray-scale GPR image of rebar in concrete. Edge detected by the Canny filter as [Fig. 1(b)] contains more curves than one, which are indistinguishable in the following hyperbola detection process, even though the noise is well suppressed. Besides, the detected result of the Canny filter will change with different manually defined thresholds. The result of the binarization method as [Fig. 1(c)] is a set of regions rather than edge curves, which are not suitable for hyperbola detections because of a wide variety of results. This paper proposed a new way to detect edges of the GPR image by collecting all the local maximum values in every A-scan data. [Fig. 1(d)] shows the binary edge image obtained in this way, which will contribute to the precise detection of hyperbola. Because for the signal image of one target, only one hyperbolic edge and a little edge of different shapes extracted from the noise left after the filtration [Fig. 1(d)]. Moreover, as no manual defined parameter is used, edges detected by this method will keep stable for any GPR data and image, which is beneficial to the stability of the final target semi-automatic detection result.

2.2. Selection of potential positions

During the process of manual detection, operators will conduct a preliminary search firstly for the whole GPR image to find the sub-areas that may contain the target, and then carry out an accurate analysis of each sub-area. This manual step can be simulated in the semi-automatic process to increase the precision and efficiency, by searching the GPR
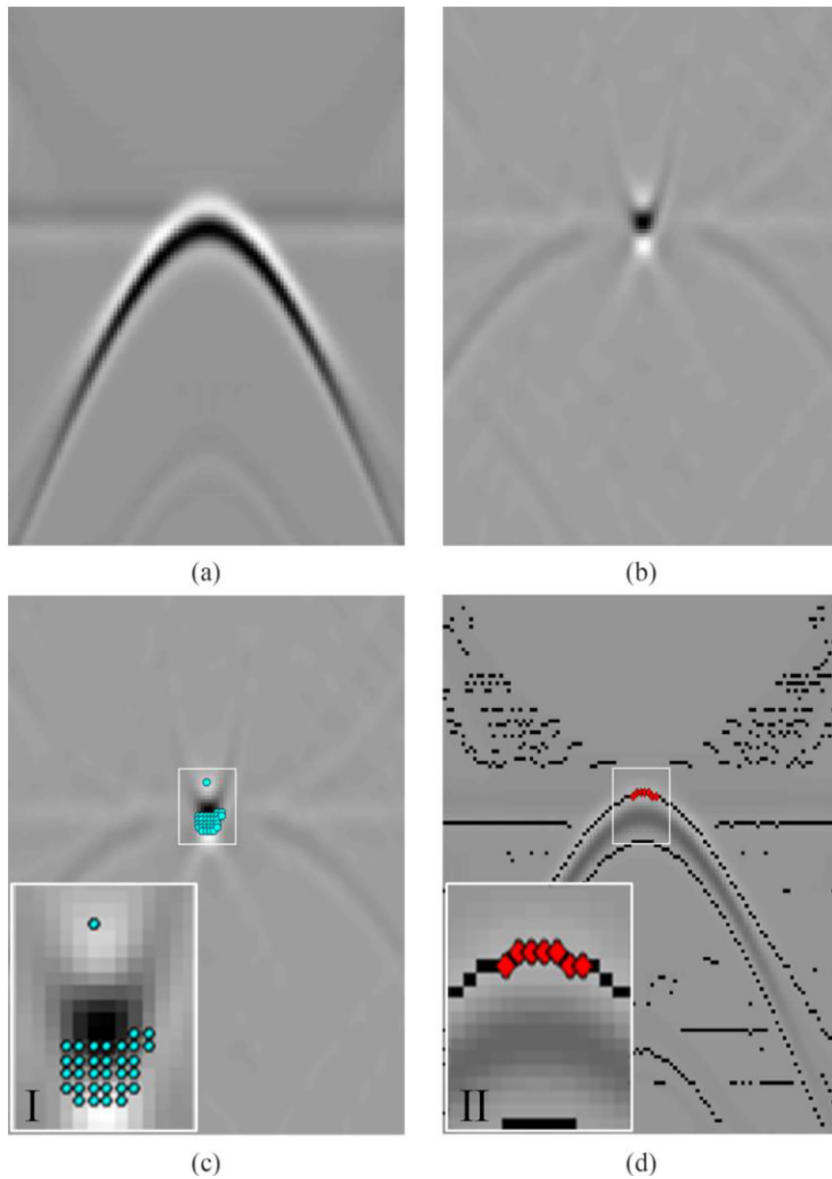
Fig. 2. Selection of potential positions based on FK migration: (a) the returned electromagnetic signal of a rebar buried in the center of concrete block, obtained by use of the FDTD method, (b) FK migration result of the simulated GPR image, (c) potential positions that be selected by comparing the vertical gray gradient with a manual defined threshold, and (d) potential positions selected eventually, marked as red diamonds, black dots are the edge of GPR image detected by collecting the local maximum points, background is the GPR image with contrast reduced. Sub-graph I and II are the magnification of center areas, to show the marks more clearly. (For interpretation of the references to colour in this figure legend, the reader is referred to the web version of this article.)

image for potential positions that may be the target. Here a simulated GPR data with no noise contained is used to illustrate the searching process of potential positions. As shown in [Fig. 2(a)], the simulated GPR image obtained by using the FDTD method [39–42], shows the return signal of a rebar buried in the center of concrete block. The diameter of the rebar is 0.05 m, the width and height of the concrete block are 1.2 m and 0.6 m, respectively. The excitation wave adopted in this paper is 800 MHz ricker-wavelet, the trace interval is 0.01 m, and total time window is 10 ns. The *dx-dy* sizes of table cell are both 0.025 m.

To reconstruct the real geometrical position of the target and find those potential positions, firstly the GPR data is processed through the FK migration [43–45], a kind of spatial deconvolution method. For discontinuous targets, amplitude or energy of the reflections will be concentrated and relatively enhanced. FK migration requires knowledge of the velocity in structure, which often makes it an interactive process [46]. Here the velocity is set to 0.1 m/ns as a simplified, which is proved to be feasible by the test results of much-measured GPR data in engineering. Firstly, the FK migration result should be normalized and transformed into a 256-gray-scale image [Fig. 2(b)], in which the reflection of target is greatly concentrated and enhanced than before. Then all potential positions can be selected by searching points with the

vertical gray gradient larger than a suitable manually defined threshold, which is assigned to be 10 in this paper. And this will achieve a better result through many parameter experiments. As the cyan dots shown in [Fig. 2(c)], 32 potential positions are obtained in total. To facilitate the design of subsequent detection algorithm and narrow the search, for every potential position the upper and lower adjacent local maximum point are selected in the same A-scan data, and the point with a larger value will be the updated potential position. In this step, 7 potential positions are selected, and all of them will distribute on the hyperbolic edge, as the red diamonds shown in [Fig. 2(d)].

3. Semi-automatic detection process

In this stage, the detection process is illustrated in detail with a field data obtained in Ci Er mountain expressway tunnel in Hebei province of China, instead of the foregoing simulated data. The field data is obtained by the ProEx RAMAC/GPR system made by Mala Geoscience Co., with a shielded antenna having a central frequency of 800 MHz, through the GPR detection to 10 rebars with a distance of 0.25 m buried in a 2.7-meter long concrete secondary lining and the depth is 0.2 m.

The field data is shown in Fig. 3 with 10 manually recognized buried rebars marked as red triangles, time in the range of 0 to 5 ns.
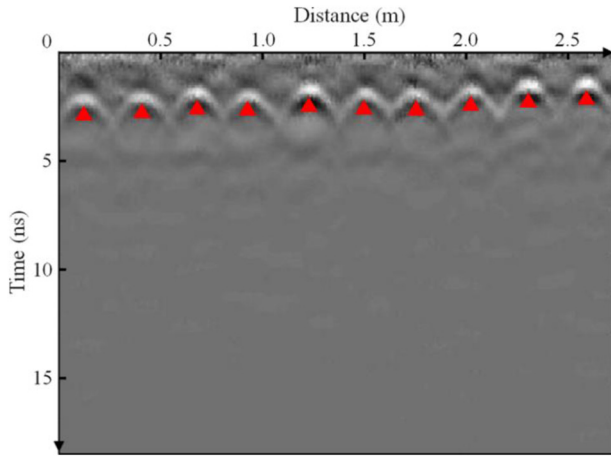
Fig. 3. Image of the field GPR data obtained in a 2.7-meter long secondary lining of Ci Er mountain expressway tunnel, 10 manually recognized buried rebars are marked as red triangles. (For interpretation of the references to colour in this figure legend, the reader is referred to the web version of this article.)

Fig. 4 is the binary edge image with potential positions, which are obtained through data preprocessing of the field data, and the potential positions are marked as black dots with red outlines. All potential positions sit near the reflection curves of targets, however, disturbed by a large amount of noise existing in GPR data. The potential positions are not only distributed on the hyperbolic edge of target reflections but also the edge of noise.

Accordingly, the following job is to find out the real targets from those potential positions, and this can be achieved by searching the best fitting hyperbola in edge image of every potential position by using GA and matching them with the hyperbolic edge of target reflections according to several carefully chosen matching criteria. The target semi-automatic detection can be achieved by the following steps in Fig. 5: create sub-windows from the binary edge image centered on every potential position with their width and height automatically calculated, time-distance relationship analysis of the target reflections, search for a best fitting hyperbola in every sub-window through GA , evaluate the

match degree between the hyperbolae and sub-windows by three criteria (Row_r, Nub_r, Dist_m), and finally divide all the hyperbolas that matching the sub-windows into categories corresponding to each buried target by the automatic classify process. Then every buried target is automatically detected by calculating the average position of hyperbola vertices in each category.

3.1. Sub-window

As the binary edge image shown in Fig. 4, reflections of targets flooded by noise seriously, are difficult to be recognized effectively by searching algorithms. Considering that the potential positions are distributed around the reflections of targets, to reduce the noise in search area, a lot of rectangular sub-windows are extracted from the edge image as new search areas, by taking each potential position (x_j, t_j) as the center. The x (m) is the distance and t (ns) is the two-way travel time of the potential target. Compared with the entire edge image, noise in sub-windows is greatly reduced while the hyperbolic edge of target reflections can be retained as much as possible. Also, an appropriate sub-window size is necessary, as the noise increases rapidly with the size increasing, but the hyperbola in the sub-window will be hard to identify if the sub-window is too small. The ideal sub-window is assumed to contain only one complete hyperbolic edge, and the height h_w (ns) and width w_w(m) of the sub-window are given as follows:

$$h_w = 1.6/f \tag{1}$$

$$w_w = Vt_j \tag{2}$$

where f is the antenna center frequency (MHz), and the wave velocity V is approximately set to 0.1 m/ns in this step. For GPR data of the same antenna frequency, heights of all sub-windows are the same, while the widths are determined by the two-way travel time of potential positions. Because the GPR signal is a data matrix with fixed unit length dx (m) in the horizontal direction and unit time dt(ns) in the vertical direction, it is more convenient to carry out the following automatic computing if the distance in horizontal and time in vertical is represented by columns and rows, respectively. Thus, the height and width of sub-window can be transformed to the number of rows and columns as follows:
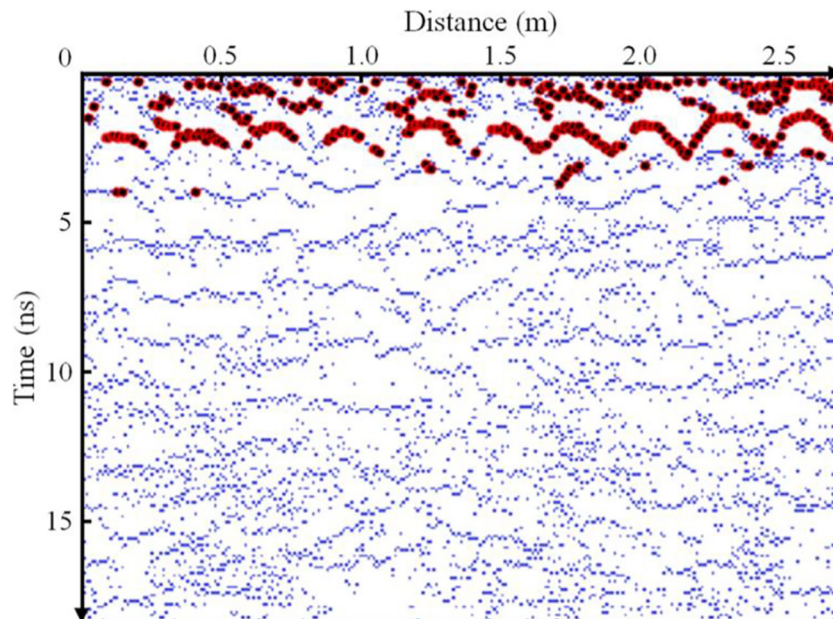

Fig. 4. Binary edge image and 389 potential positions obtained by data preprocessing, and the potential positions are marked as black dots with red outlines. (For interpretation of the references to colour in this figure legend, the reader is referred to the web version of this article.)
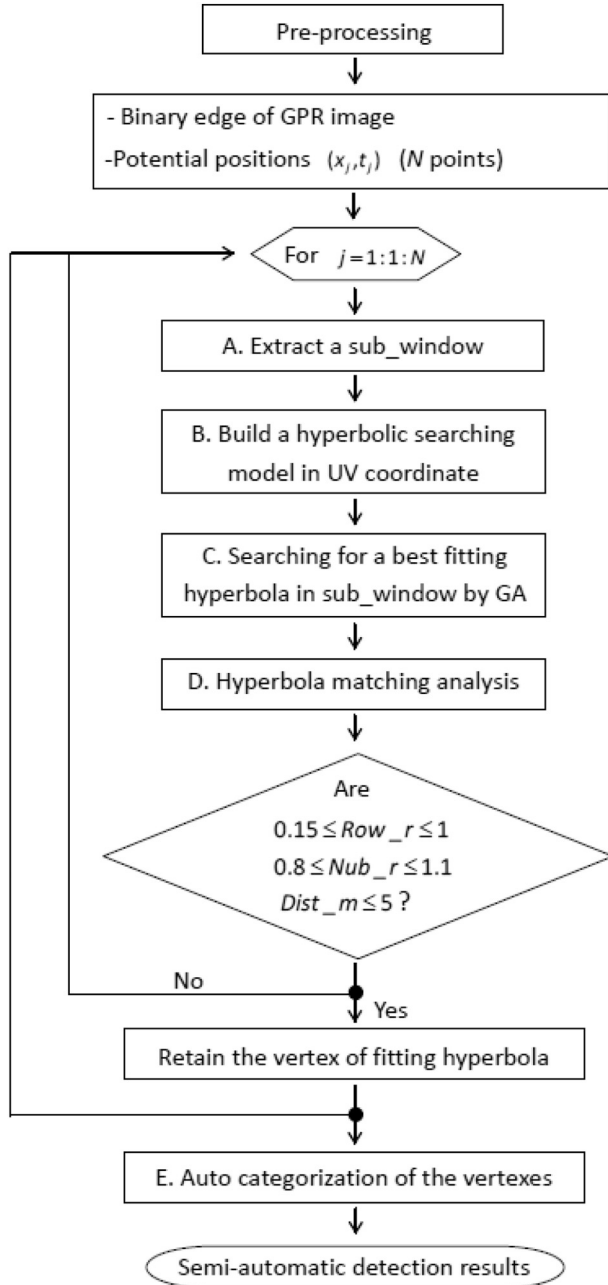
Fig. 5. Flowchart of the semi-automatic detection process.

$$Row\_sw = 2 \cdot \left[\frac{h_w}{2 \cdot dt} \right] + 1 \tag{3}$$

$$Col\_sw = 2 \cdot \left[\frac{w_w}{2 \cdot dx} \right] + 1 \tag{4}$$

where Row_sw stands for the number of rows in the sub-window, and Col_sw is the number of columns. Furthermore, as the bracket stands for an integral function, both Row_sw and Col_sw are limited to odd numbers.

Two examples of sub-window are shown in Fig. 6, including one with the potential positions distributing on the edge of noise, and the other with the potential positions distributing on the edge of target reflections. Hyperbolic edges are marked as black to distinguish from the noise, and the potential position is at the center of sub-window, represented by intersection of the horizontal and vertical dotted lines. Sub-windows correspond to potential positions distributing on noise

[Fig. 6(a)] are mainly composed of noise, with little or no hyperbolic edge included. The hyperbolic edge in sub-windows with potential positions distributing on the target reflections [Fig. 6(b)] is prominent compared with the former, which is easier to be identified.

3.2. Time-distance relationship

After getting the sub-windows, the time-distance relationship of hyperbolic target reflections is analyzed to build a mathematical hyperbola model for the next GA searching process. In ideal conditions, signals reflected from the buried targets will be recorded by the receiving antenna, and can be described by a function of distance and travel time. The medium is evenly distributed around the target in the simulation experiment that studied before. Therefore, it is assumed that the medium around is uniform, and the hyperbolic edge detected from the reflection of target [Fig. 7] can be described as follow:

$$Vt_i = \sqrt{H^2 + (x_0 - x_i + d)^2} + \sqrt{H^2 + (x_0 - x_i)^2} \tag{5}$$

where V is the wave velocity in medium (m/ns), (x_0, H) is position (m) and depth (m) of the target, (x_i, t_i) stands for the position and two-way travel time (ns) of a point i on the edge and d is the distance of the transmit antenna and the receiving antenna (m). Assume the distance d to be zero, Eqs. (6) and (7) can be derived from Eq. (1):

$$t_0 = 2H/V \tag{6}$$

$$Vt_i = 2\sqrt{(Vt_0/2)^2 + (x_0 - x_i)^2} \tag{7}$$

where t_0 is the two-way travel time (ns) corresponding to the depth H. Moreover, Eq. (7) can be further transformed into a standard hyperbola function:

$$t_i^2/t_0^2 - 4(x_0 - x_i)^2/(Vt_0)^2 = 1 \tag{8}$$

That is, the hyperbolic edge in binary GPR image follows a standard hyperbola function shown in Eq. (8) under ideal conditions when we neglect the radius of the target and the antenna distance. Also, as the wave velocity V depends mostly on the relative permittivity ε_r of the homogeneous medium around, the hyperbolic edge is defined once the position, depth of target and medium type are determined.

However in field detections, the hyperbolic edge can hardly be a perfect shape as the return signal recorded is distorted with a variety of factors such as surface interference, bounce, slip and uneven moving speed of the antenna, etc. Distortions usually appear as the dissymmetry [Fig. 8(a)], discontinuous [Fig. 8(b)] in branches of hyperbola, and cross-interference [Fig. 8(c)] when targets are densely distributed. Therefore, distortion of the hyperbola must be taken into account in the following steps while detecting the hyperbolae in binary image to ensure the expected precision.

3.3. Hyperbolic edge detection in sub-window

As mentioned above, the size of the sub-window is designed to contain only one hyperbolic edge of target reflection. And in this step, this edge can be detected using GA, if the hyperbolic feature in the sub-window is notable enough. The sub-window is treated as an UV picture, and the pixel in it is located by its column and row (u, v), which can be converted to the horizontal distance and two-way travel time (x, t) by:

$$x = x_i + [u - (Col\_sw + 1)/2] \cdot dx \tag{9}$$

$$t = t_i + [v - (Row\_sw + 1)/2] \cdot dt \tag{10}$$

where (x_i, t_i) is the horizontal distance and two-way travel time of the sub-window center corresponding to the potential position of point i.

GA is a well-known method searching the optimal solution by mimicking the biological evolutionary mechanism in Darwin's theory. Also GA is a very effective and stable choice compared with the conventional methods for many complex problems, especially the
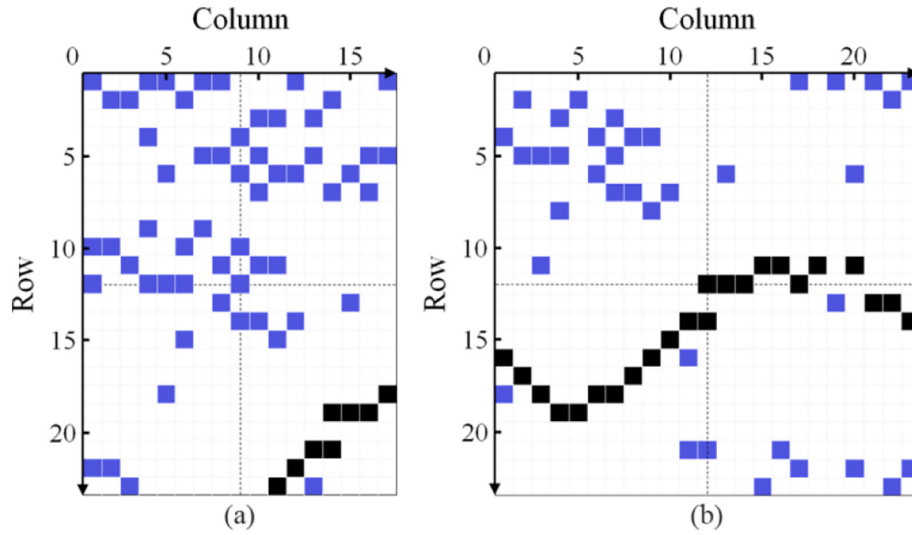
Fig. 6. Two kinds of sub-windows isolated from the binary image, the hyperbolic edge is marked as black, and the potential position is represented by intersection of dotted lines at the center of sub-window.
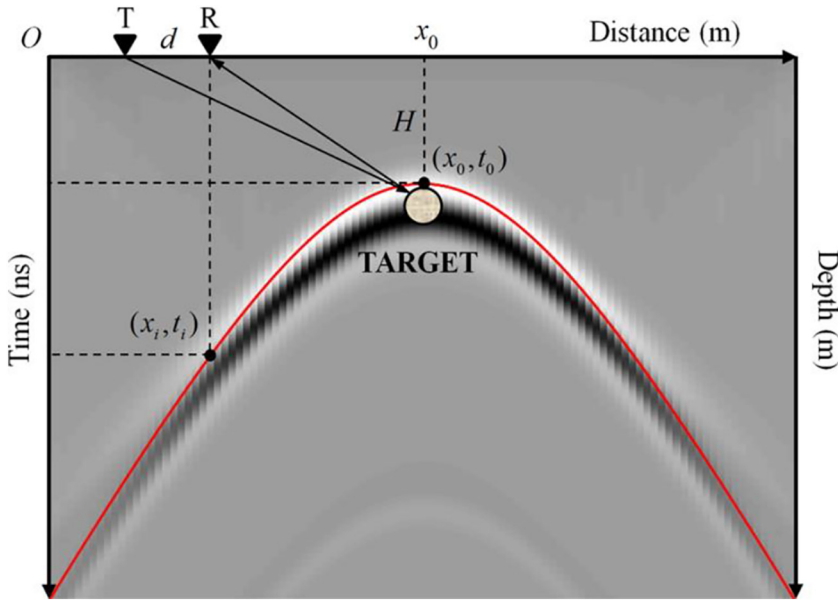

Fig. 7. Time-distance relationship of the hyperbolic edge of target reflection, the letter T and R represent the transmit antenna and the receiving antenna, and the red curve is the hyperbolic edge detected from the reflection of the target. (For interpretation of the references to colour in this figure legend, the reader is referred to the web version of this article.)

optimization problems [47–50]. The chromosome is always encoded in some fashion, so the input value of GA may be a set of potential solutions. In addition, a criterion called fitness function that requires each candidate to be quantitatively evaluated. According to the result of the evaluation of each candidate, and the promising candidates are kept and allowed to reproduce with some random changes. Then these digital offspring go on to the next generation and form a new pool of candidate solutions, which are subjected to a second round of fitness evaluation. Very good solutions to the problem can lastly be discovered in an iterative process [51].

The hyperbolic edge is detected by searching for a best fitting hyperbola which covers the most edge pixels in sub-window by GA. Firstly
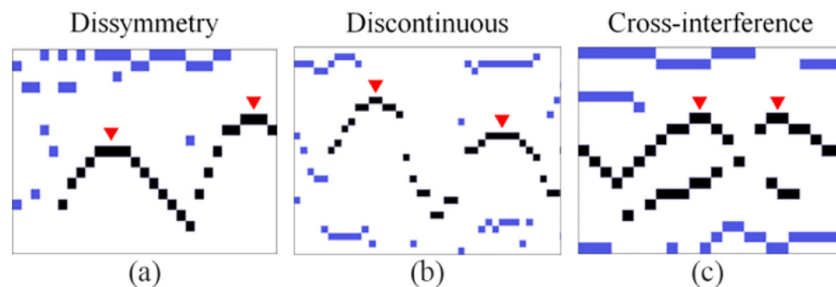

Fig. 8. Distortions of the returned signal, hyperbolic edge of the target reflections is marked as black, the edge of the noise is marked as blue, and the red triangle shows the vertex of the hyperbolic edge. (For interpretation of the references to colour in this figure legend, the reader is referred to the web version of this article.)
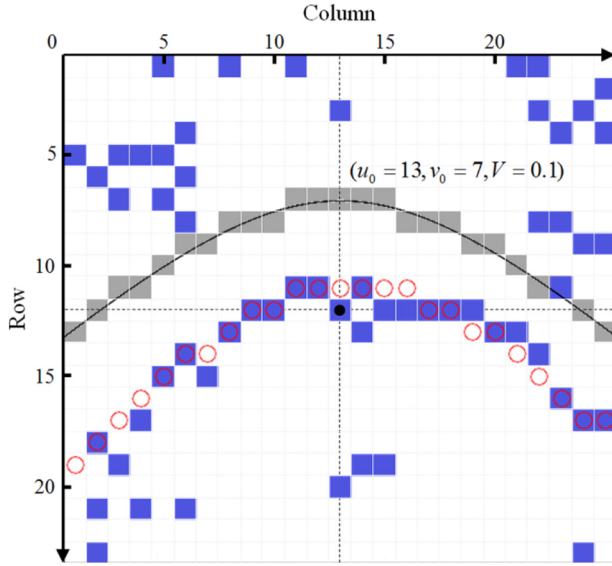
Fig. 9. Sub-window of the 20th potential position, the potential position is marked as a black dot at the center, blue rectangles are the signal edges, black curve is the hyperbola model with the parameters as (13, 7, 0.1), the gray rectangles are the pixels covered by this hyperbola. A best-fitting hyperbola which covers the most edge pixels is detected with the parameters as (13, 12, 0.091) through GA, and the edge pixels covered by it are marked as red circles. (For interpretation of the references to colour in this figure legend, the reader is referred to the web version of this article.)

Fig. 10. Matching region defined by expanding the hyperbola up and down both by one row, hyperbola searched by GA is marked as red circle, and boundary of the matching region is marked as black dotted line in bold, $SB1$ and $SB2$ are sub-windows centered by (u_c, v_c) and (u'_c, v'_c), and the red dotted lines show the upper and right boundary of $SB2$. (For interpretation of the references to colour in this figure legend, the reader is referred to the web version of this article.)

a hyperbola model is established in the sub-window based on Eq. (8), in which a searched hyperbola is completely defined by three parameters: the UV coordinates of the hyperbola vertex (u, v) and wave velocity V. Taking sub-window of the 20th potential position as an example, when parameters (u, v, V) are assigned to the value of (13, 7, 0.1), the searched hyperbola and pixels it covers are shown in Fig. 9. Three parameters of the hyperbola model are taken as genes composed of an 8-bit binary number. Each gene assumes a real value within the interval $u \in [1, Row\_sw]$, $v \in [1, Col\_sw]$ and $V \in (0, 0.3)$. The initial population is composed of 20 randomly generated individuals, the stochastic universal sampling method [48–50] is used in the chosen operation with the crossover rate as 0.9 and the mutation rate as 0.1, and the adopted fitness function is the number of edge pixels uncovered by the searched hyperbola. The crossover and mutation rate determine the frequency of crossover and mutation operation, respectively.

When the crossover rate is too large, the excellent individuals in the population are more likely to be destroyed, so that there is a big difference with the last generation and the genetic search becomes randomly. However, if it is too low, more individuals will be directly copied to the next generation and the genetic search may be stalled or trapped in a local optimal solution. Normally, the crossover rate ranges from 0.4 to 0.99. When the mutation rate is too high, more new individuals can be generated to increase the diversity of individuals in the population, but it is also easy to damage the excellent individuals and make the genetic search go to randomization. When it is too low, the genetic search is also easy to fall into the local optimal solution. So, the general variation rate can be selected in the range of 0.0001 to 0.1.

We have carried out lots of experiments on the effect of genetic generations (from 0 up to 150) to the experimental results, and found that by the 74th generation, a hyperbola highly matching the target signal had been obtained through GA. The experiment continued until the 150th generation, and the experimental results were consistent with the 74th generation. In this paper, the conservative value 150 was selected to strive for the optimal solution obtained by each calculation to be the actual accurate solution. After 150 generations of genetic computation, the best fitting hyperbola is detected with the parameters as
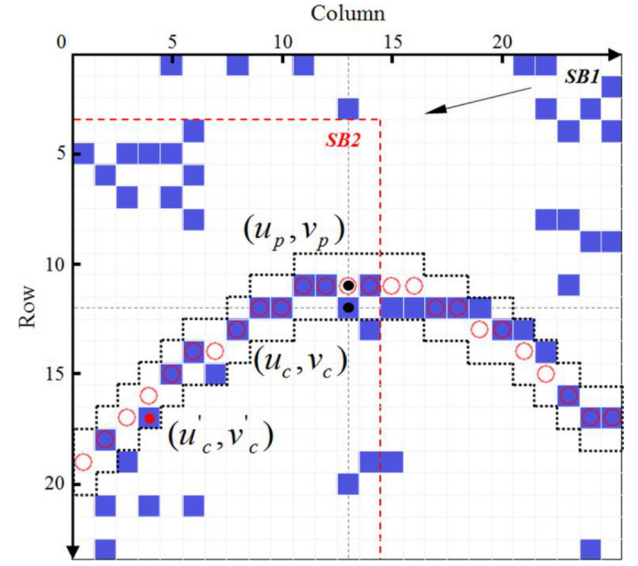
(13, 12, 0.091), which is marked as red circles shown in Fig. 9.

3.4. Hyperbola matching analysis

As for potential positions distributing on the edge of noise, only little or no hyperbolic edge is included in their sub-window, which is hard to be detected by searching for a best fitting hyperbola that covers the most edge pixels. Even for potential positions that distributing on the edge of target reflections, with the hyperbolic edge in the sub-window complete and prominent, the hyperbola that searched by GA may not be in agreement with the hyperbolic edge, because the result of GA is not an exact solution, and it is affected by the noise of edge around.

In this step, several criteria are designed to analyze the match degree between the fitting hyperbola and the hyperbolic edge in every sub-window, the corresponding potential position is retained only when the fitting hyperbola matches the hyperbolic edge. Considering the waveform distortion in field GPR data, a matching region is defined firstly by expanding the hyperbola up and down both by one row, as the black dotted line in bold shown in Fig. 10. (u_c, v_c) is the potential position at the center, (u_p, v_p) is the vertex of hyperbola searched by GA, and the pixels covered by the hyperbola are marked as red circles. Based on the observation and analysis of the detection data with a length of nearly 21 km, we studied the characteristics of target hyperbolic, clutter hyperbolic, waveform distortion and other factors in the measured data, and thus proposed three criteria for the prediction hyperbolic. At the same time, we extracted about 100 representative sub-windows from the measured data for research, and finally determined the effective value range of each criterion.

3.4.1. Row_r

Compare the number of rows that occupied by the fitting hyperbola (DC_{row}) with the rows of sub-window (Row_sw):

$$Row\_r = DC_{row}/Row\_sw \tag{11}$$

The variable Row_r theoretically ranges in the interval $Row\_r \in (0,1]$, and a smaller value stands for a more gently hyperbola. By setting a

suitable lower bound of Row_r, this criterion is designed mainly to avoid the influence of straight noise, which is common in the shallow part of the GPR image. However, the correct matching of the hyperbolic edge will be missed if the lower bound is assigned to a large value. This paper accepts Row_r values varying from 0.15 to 1.

3.4.2. Nub_r

Compare the number of pixels in the matching region (PN_{model}) with the number of grids that be covered by the fitting hyperbola (PN_{data}):

$$Nub\_r = PN_{model}/PN_{data} \tag{12}$$

The variable $Nub\_r \in [0, 3]$ indicates the match degree of the hyperbolic edge and the fitting hyperbola. For the $Nub\_r \in [0,1)$, the match degree get higher with the increasing of Nub_r, and when the hyperbola matches the hyperbolic edge ideally, Nub_r equals to 1 as the hyperbolic edge all fall in the matching region and no edge with noise is included at the same time. And for the Nub_r far greater than 1, the matching region is mainly filled with the dense edges with noise instead of the hyperbolic edges, which manifests that the hyperbola does not match the hyperbolic edge. Here Nub_r is accepted in the range of 0.8 to 1.1.

3.4.3. Dist_m

The more hyperbolic edges contained in the sub-window, the more accurate the hyperbola detected by GA matches the hyperbolic edge. For potential positions that distributing on the hyperbolic edge and near the vertex, such as (u_c, v_c) shown in Fig. 10, the major part of the hyperbolic edge is included in sub-window $SB1$, and the hyperbola matches the hyperbolic edge. While in sub-window $SB2$ centered by potential position (u'_c, v'_c), only the left half of this hyperbolic edge is included. Hyperbola detected by GA in $SB2$ is matched with the left half of this hyperbolic edge under the first 2 criteria, but it is very different from the hyperbola detected in $SB1$, as not being confined by the right half of the hyperbolic edge during the GA detection. This can be avoided by setting an upper limit of the pixel distance $Dist\_m$ from the vertex of the hyperbola (u_p, v_p) to sub-window center (u_c, v_c):

$$Dist\_m = \sqrt{(u_p - u_c)^2 + (v_p - v_c)^2} \tag{13}$$

This paper accepts $Dist\_m$ less than or equal to 5. In this way, hyperbolas that matching the same hyperbolic edge will be similar.

3.4.4. Auto-categorization

Retaining all the vertexes of matching hyperbolas as the fitting points, they will gather around every vertex of the hyperbolic edges as the matching hyperbolas for one target are similar. All the fitting points will be classified into several categories according to the horizontal distance $Ld_{i,j}$ and longitudinal time distance $Td_{i,j}$ between them, assuming N to be the total number of fitting points and $i, j = 1,2,3, …,N$. For fitting positions in the same category, $Ld_{i,j}$ and $Td_{i,j}$ meet the requirements shown in Eqs. (14) and (15):

$$Ld_{i,j} \leq 0.5d_{es} \tag{14}$$

$$Td_{i,j} \leq 1.1/f \tag{15}$$

where d_{es} is an estimated target spacing (m), and f is the antenna central frequency (MHz). After this auto-categorization procedure, final points are generated by taking the average position of fitting points in each category. And the final points are the semi-automatic detection results of the buried targets.

The semi-automatic detection result of the test example in the Ci Er mountain tunnel is shown in Fig. 11, in which the fitting points are marked as red dots and 12 final points obtained after the auto-categorization are marked as black circles. All 10 rebars are correctly detected, but 2 misjudged points are also generated at distance 0.33 m and 0.52 m.
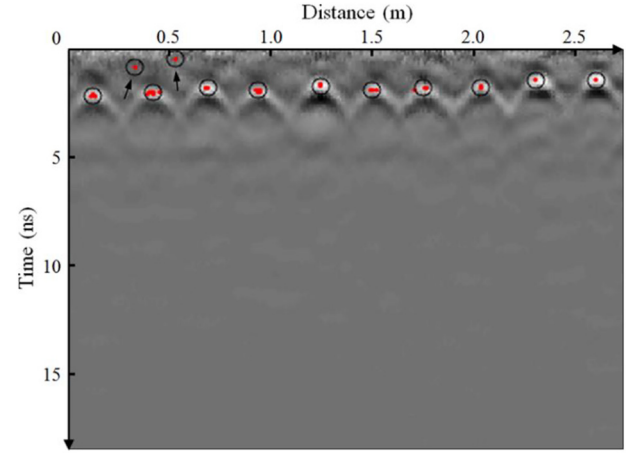

Fig. 11. Semi-automatic detection result of the test example in the Ci Er mountain tunnel, the fitting points are marked as red dots, and 12 final points are marked as black circles, including 2 misjudged points at distance 0.33 m and 0.52 m, marked by black arrows. (For interpretation of the references to colour in this figure legend, the reader is referred to the web version of this article.)

4. Practical application

4.1. Precision analysis

Semi-automatic detection of four measured GPR data with different frequency antennas and detection objects in expressway tunnel is introduced in this part to analyze the limitation and precision of the semi-automatic method through comparing with the manual detection results. These data are collected by the ProEx RAMAC/GPR system same as above made by Mala Geoscience Co., and different frequency antennas are shown in Fig. 12.

The first data is obtained by 500 MHz shielded antenna in a 1.2-kilometer-long expressway tunnel in Hebei province of China, through the GPR detection to 33 rebars with the distance of 0.25 m buried in an 8.59-meter-long secondary lining by concrete at a depth of 0.2 m. The second data is obtained by 800 MHz shielded antenna in a 0.7-meter-long expressway tunnel in the Shanxi province of China, through the GPR detection to 11 steel arches with the distance of 1 m buried in a 10.44-meter-long initial lining by concrete at a depth of 0.2 m. The third data is obtained by 1000 MHz shielded antenna in a 5.1-kilometer-long expressway tunnel in the Shanxi province of China, through the GPR detection to 33 rebars with the distance of 0.25 m buried in a 7.30-meter-long secondary lining by concrete at a depth of 0.1 m. The fourth data is obtained by 1600 MHz High Frequency (HF) antenna in a 1.8-kilometer-long expressway tunnel in the Yunnan province of China, through the GPR detection to 34 rebars with the distance of 0.25 m buried in an 8.80-meter-long secondary lining by concrete at a depth of 0.2 m. A brief description of these four data is shown in Table 1, in which the number of targets is obtained by the manual detection process.

The semi-automatic detection results are shown in Fig. 13, as well as the B-scan image and binary image of each data. Besides, only a shallow part of every image is displayed here, showing the reflections of targets more clearly. All final points obtained by the semi-automatic detection algorithm are marked as cyan rhombi or red circles, where the former indicates a correct detection and the latter represents a misjudgment.

The detection results of D1 are shown in [Fig. 13(a) and (b)], 390 potential positions or sub-windows are obtained after the FK migration process and the filtration based on gray gradient. After that, the detection process is carried out in each sub-window, and 34 final points are generated by the finally auto-categorization process. Through the comparison of semi-automatic and manual results, we can see that 29 of
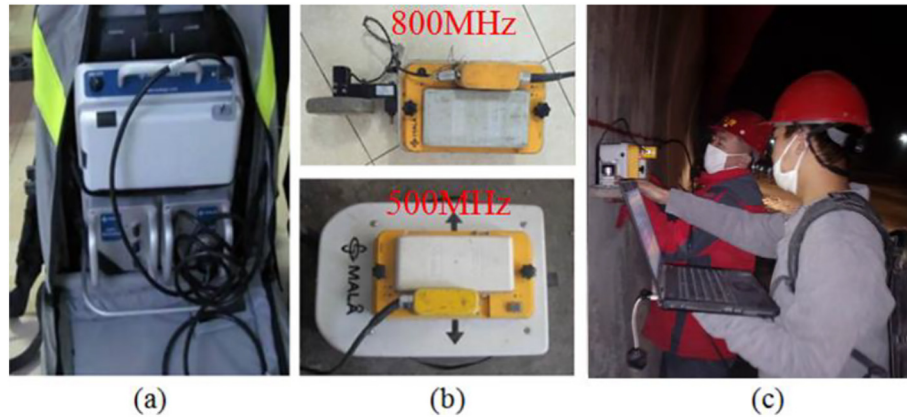
Fig. 12. Semi-automatic detection process and radar collecting equipment, (a) is the RAMAC/GPR CUIII Host made by Mala Geoscience Co.; (b) contains the 800 and 500 MHz shielded antennas adopted in our experiment; (c) is the experiment data collection process at the scene of tunnels.

Table 1
Information of measured data.

No.	Frequency (MHz)	Object	Distance (m)	Number of targets
D1	500	Secondary lining	8.59	33
D2	800	Initial lining	10.44	11
D3	1000	Secondary lining	7.30	33
D4	1600	Secondary lining	8.80	34

Table 2
Semi-automatic detection results of the measured data.

No.	Number of targets	Final position	Missed rate (%)	Misjudgment rate (%)	Computing time (s)
D1	33	34	12.1	15.2	107
D2	11	13	0	18.2	238
D3	33	28	15.2	0	226
D4	34	27	20.6	2.9	251

the 33 buried rebars in this data are correctly identified by the semi-automatic algorithm, accompanied by 4 left undetected and 5 misjudged. Therefore, the undetected rate is 12.1% and the misjudgment rate is 15.2%. As can be seen in [Fig. 13(b)], 3 undetected targets and 3 misjudged positions concentrated in the distance range of 3–4 m, and the GPR signals in this area are highly ill-shaped simultaneously, which indicates that concrete of the secondary lining in this area is not compact. Thereby damages in concrete around the targets will affect the accuracy of semi-automatic detection results. [Fig. 13(c) and (d)] show the detection results of D2, of which 13 final points are totally semi-automatic detected, including 11 positions correctly identified and 2 misjudged. The undetected rate is 0 and the misjudgment rate is 18.2%. And for D3, as shown in [Fig. 13(e) and (f)], 28 final points are generated by the semi-automatic algorithm with no misjudgments and 5 rebar undetected. The undetected rate is 15.2% and the misjudgment

rate is 0. And for D4 [Fig. 13(g), (h)], 27 final points are semi-automatically generated with 1 position misjudged and 26 positions correctly identified, corresponding to 7 undetected targets. The undetected rate is 20.6% and the misjudgment rate is 2.9%. Table 2 summarizes the semi-automatic detection results of the four measured GPR data. The detection result is ideal since the average undetected rate is 11.98% and the average misjudgment rate is 9.08%.

4.2. Further research

The same GPR profile of secondary lining with different frequency antennas from Hong Hua Liang tunnel in Hebei province of China, is detected again to further verify the relationship between antenna central frequency and detection precision. Four measured data are respectively obtained by 500/800/1000/1600 MHz shielded antennas in

Fig. 13. Semi-automatic detection results of the measured data with different antenna central frequencies and objects, (a) and (b) are results of the 500 MHz secondary lining GPR data; (c) and (d) are results of the 800 MHz initial lining GPR data; (e) and (f) are results of the 1000 MHz secondary lining GPR data; (g) and (h) are results of the 1600 MHz secondary lining GPR data; the correctly detected targets are marked as cyan diamonds, and the misjudged targets are marked as red dots. (For interpretation of the references to colour in this figure legend, the reader is referred to the web version of this article.)
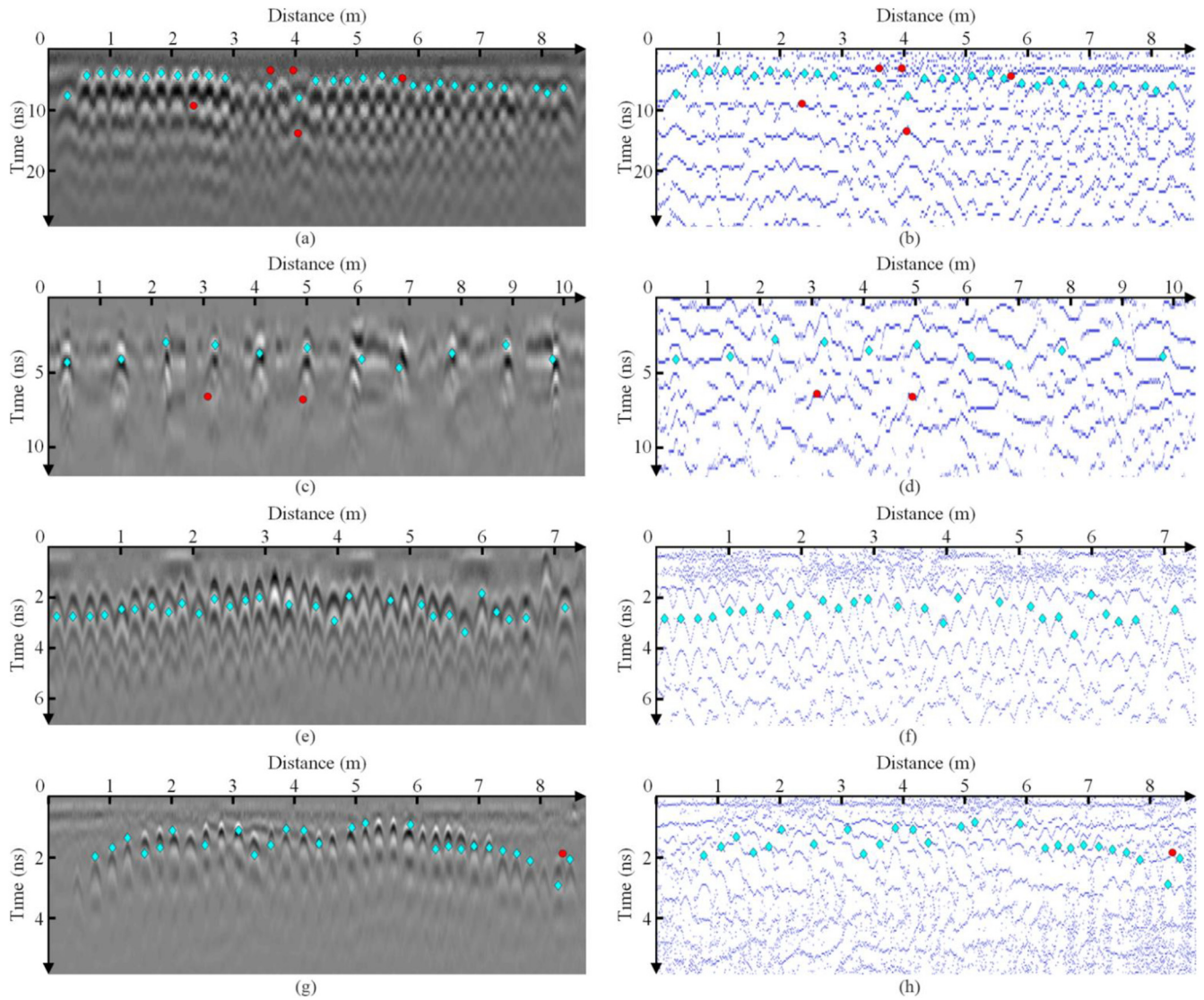
Fig. 14. The process of collecting secondary lining GPR data with different frequency antennas in Hong Hua Liang tunnel.

Table 3
Information of measured data.

No.	Frequency (MHz)	Object	Distance (m)	Number of targets
D5	500	Secondary lining	7.92	40
D6	800	Secondary lining	7.97	40
D7	1000	Secondary lining	7.97	40
D8	1600	Secondary lining	7.98	40

a 4.4-kilometer-long tunnel in Hebei province of China, through the GPR detection to 40 rebars with a distance of 0.2 m buried in an 8-meter-long secondary lining by concrete at a depth of 0.1 m. The length of collected data may be a slight deviation compared to the measured data with 8 m, due to the operation and response of workers, but this has little effect to the experimental results. The process of collecting secondary lining GPR data with different frequency antenna in Hong Hua Liang tunnel is shown in Fig. 14. A brief description of these four data is shown in Table 3, in which the number of targets is obtained by the manual detection process.

The semi-automatic detection results are shown in Fig. 15, as well as the B-scan image of each data. All final points obtained by the semi-automatic detection algorithm are marked as cyan rhombi or red circles, where the former indicates a correct detection and the latter represents a misjudgment. Table 4 summarizes the semi-automatic detection results of the four measured GPR data, and the detail of every measured GPR data isn't shown in the article again.

The detection results of D5 are shown in Fig. 15(a), and 38 final points are generated by the finally auto-categorization process. Through the comparison of semi-automatic and manual detection results, we can see that 32 of the 40 buried rebars are correctly identified by the semi-automation algorithm, accompanied by 8 left undetected and 6 misjudged. Therefore, the undetected rate is 20% and the misjudgment rate is 15%. But the later three data all can get a high precision while detecting the rebars buried in the secondary lining compared with the D5. The detection results of D8 are shown in Fig. 15(d), we can see that 39 of the 40 buried rebars are correctly identified by the semi-automation algorithm, accompanied by 2 left undetected and 1 misjudged. Moreover, the missed rate of this semi-automatic algorithm decreases with the increasing of antenna central frequency, when the misjudgment rate remains stable. Therefore, in practical detection applications, the antenna with higher frequency should be selected according to the approximate buried depth of the target to obtain higher identification accuracy. The computer, with an Intel Core i5-750 CPU, 4G memory, 64-bit window10 operating system and a MATLAB environment in it, is used for all the cases above.
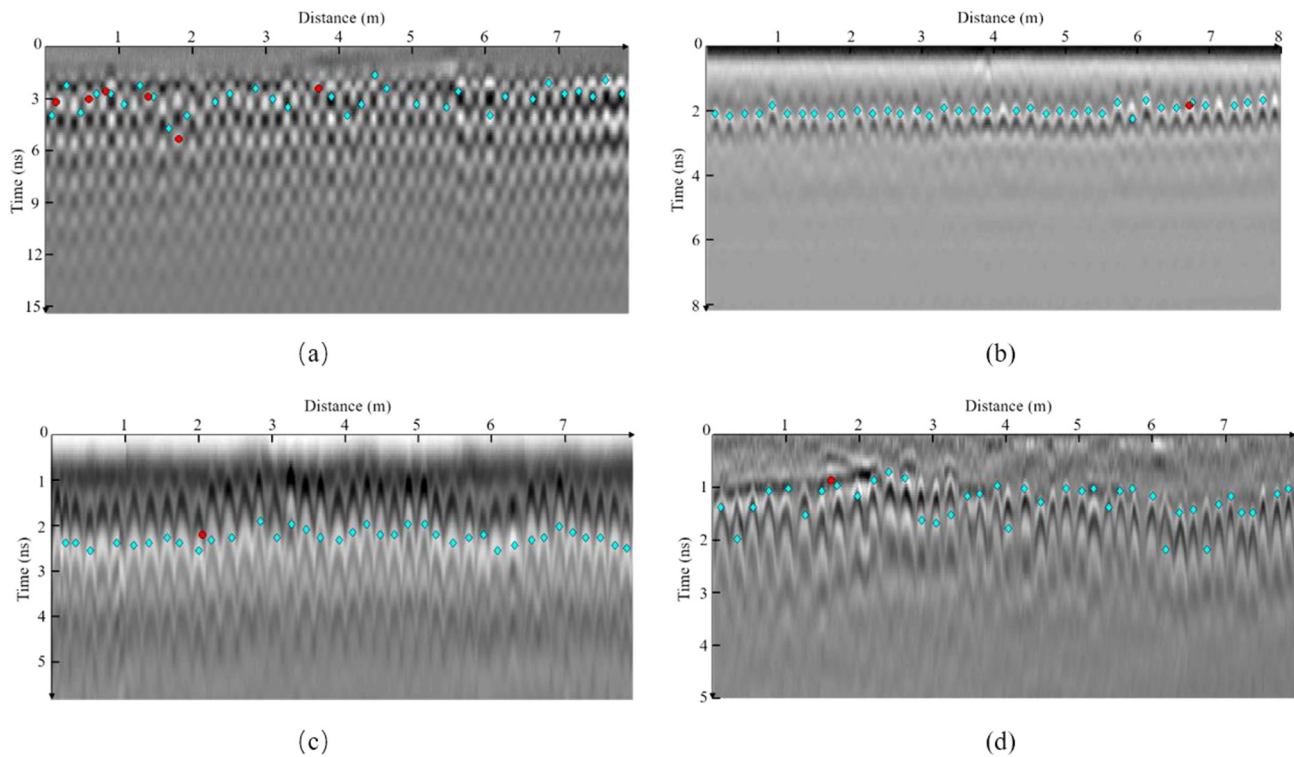
Fig. 15. Semi-automatic detection results of the same measured GPR data with different central frequency antennas, (a) is result of the 500 MHz secondary lining GPR data; (b) is result of the 800 MHz secondary lining GPR data; (c) is result of the 1000 MHz secondary lining GPR data; (d) is result of the 1600 MHz secondary lining GPR data; the correctly detected targets are marked as cyan diamonds, and the misjudged targets are marked as red dots. (For interpretation of the references to colour in this figure legend, the reader is referred to the web version of this article.)

Table 4
Semi-automatic detection results of the measured data.

No.	Number of targets	Final position	Missed rate (%)	Misjudgment rate (%)	Computing time (s)
D5	40	38	20	15	382
D6	40	38	7.5	2.5	242
D7	40	38	7.5	2.5	259
D8	40	39	5	2.5	275

5. Conclusion

This paper presented a new algorithm for semi-automatic detection of buried rebars in GPR data to overcome the inefficiency and instability problems in the manual recognition process, especially for complex GPR surveys with a large quantity of data. Based on the hyperbolic feature of signal reflected from the discrete target, this algorithm firstly includes a preprocessing step, the generating of a binary image by collecting all the local maximum points in GPR data, and the semi-automatic selecting of all potential positions of targets by FK migration and gray gradient filtration. The main processes of this algorithm include the fitting hyperbola detecting using GA in sub-windows centered by potential positions, matching of the hyperbolas with the hyperbolic edges by three criteria chosen on the basis of a large number of experiments and calibrations, and finally the generation of final points by auto-categorization of the fitting hyperbolas.

Four measured data of different central frequency antennas and detection objects in expressway tunnel are used to verify the precision of this semi-automatic algorithm. The average undetected rate of 11.98% and misjudgment rate of 9.08% prove the applicability and precision of this algorithm in the semi-automatic detection of rebar buried in concrete.

Meanwhile, four central frequency antennas are used to detect the

same GPR data of secondary lining in Hong Hua Liang tunnel, and the results show that the missed rate of semi-automatic detection decreases with the increase of the antenna frequency, when the misjudgment rate remains stable. The antenna with higher frequency should be selected according to the approximate buried depth of the target to obtain higher identification accuracy in the practical detection applications according to our experiment.

Declaration of competing interest

The authors declare that they have no known competing financial interests or personal relationships that could have appeared to influence the work reported in this paper.

References

[1] D.X. Li, Methods and Applications of Ground Penetrating Radar, 1st ed., 12 Geological Publishing House, China, 7-116-01771-2, 1994.

[2] D.J. Daniels, Ground Penetrating Radar, 2nd ed, The Institution of Electrical Engineers, England, 2005.

[3] A. Atef, T. Zayed, A. Hawari, M. Khader, O. Moselhi, Multi-tier method using infrared photography and GPR to detect and locate water leaks, Autom. Constr. 61 (2016), https://doi.org/10.1016/j.autcon.2015.10.006.

[4] P. Szymczyk, M. Szymczyk, Non-destructive building investigation through analysis of GPR signal by S-transform, Autom. Constr. 55 (2015) 35–46, https://doi.org/10.1016/j.autcon.2015.03.022.

[5] S. Yilmaz, Ç. Balkaya, O. Çakmak, E. Oksumaetc, GPR and ERT explorations at the archaeological site of Kılıç village (Isparta, SW Turkey), J. Appl. Geophys. 170 (2019) 103859, https://doi.org/10.1016/j.jappgeo.2019.103859.

[6] D. Angelis, P. Tsourlos, G. Tsokas, G. Vargemezis, G. Zacharopoulou, C. Power, Combined application of GPR and ERT for the assessment of a wall structure at the Heptapyrgion fortress (Thessaloniki, Greece), J. Appl. Geophys. 152 (2018) 208–220, https://doi.org/10.1016/j.jappgeo.2018.04.003.

[7] M. Solla, H. Lorenzo, F.I. Rial, A. Novo, Ground-Penetrating Radar for the structural evaluation of masonry bridges: results and interpretational tools, Constr. Build. Mater. 29 (2012) 458–465, https://doi.org/10.1016/j.conbuildmat.2011.10.001.

[8] H. Qin, X. Xie, J.A. Vrugt, K. Zeng, G. Hong, Underground structure defect detection and reconstruction using crosshole GPR and Bayesian waveform inversion, Autom.

Constr. 68 (2016) 156–169, https://doi.org/10.1016/j.autcon.2016.03.011.

[9] K. Dinh, T. Zayed, S. Moufti, A. Shami, A. Jabri, M. Abouhamad, T. Dawood, Clustering- based threshold model for condition assessment of concrete bridge decks using Ground Penetrating Radar, Transportation Research Record: Journal of the Transportation Research Board. 2522 (2015) 81–89, https://doi.org/10.3141/2522-08.

[10] S.A. Dabous, S. Yaghi, S. Alkass, O. Moselhi, Concrete bridge deck condition assessment using IR thermography and Ground Penetrating Radar technologies, Autom. Constr. 81 (2017) 340–354, https://doi.org/10.1016/j.autcon.2017.04.006.

[11] T. Saarenketo, T. Scullion, Road evaluation with Ground Penetrating Radar, J. Appl. Geophys. 43 (2–4) (2000) 119–138, https://doi.org/10.1016/S0926-9851(99)00052-X.

[12] M. Varela-González, M. Solla, J. Martínez-Sánchez, P. Arias, A semi-automatic processing and visualization tool for Ground-Penetrating Radar pavement thickness data, Autom. Constr. 45 (2014) 42–49, https://doi.org/10.1016/j.autcon.2014.05.004.

[13] S.H. Zhong, H.Z. Sun, F. Yang, J. Liu, R. Wang, Geological Exploration and Detection Technology of Ground Penetrating Radar, 1st ed., Shanghai Science & Technology Publishers, China, 2016 (ISBN: 978-7-5478-2909-7/TN.18).

[14] F.A. Romero, C.L. Barnes, H. Azari, S. Nazarian, C.D. Rascoe, Validation of benefits of automated depth correction method: improving accuracy of Ground-Penetrating Radar deck deterioration maps, Transportation Research Record: Journal of the Transportation Research Board. 2522 (1) (2015) 100–109, https://doi.org/10.3141/2522-10.

[15] H. Feng, Z. Zeng, S. Liu, GPR Signal Processing, 1st ed., Science Press, China, 978-7-03-042418-1, 2014.

[16] F.J. Prego, M. Solla, X. Núñez-Nieto, P. Arias, Assessing the applicability of ground penetrating radar to quality control in tunneling construction, J. Constr. Eng. M. 142 (5) (2016), https://doi.org/10.1061/(ASCE)CO.1943-7862.0001095.

[17] I. Qader, F. Amara, O. Abudayyeh, Fractals and independent component analysis for defect detection in bridge decks, Adv. Civ. Eng. 2011 (1) (2011) 1–14, https://doi.org/10.1155/2011/506464.

[18] E. Pasolli, F. Melgani, M. Donelli, Automatic analysis of GPR images: a pattern-recognition approach, IEEE Trans. Geosci. Remote Sens. 47 (7) (2009) 2206–2217, https://doi.org/10.1109/TGRS.2009.2012701.

[19] W. Al-Nuaimy, Y. Huang, M. Nakhkash, M.T.C. Fang, V.T. Nguyen, A. Eriksen, Automatic detection of buried utilities and solid objects with GPR using neural networks and pattern recognition, J. Appl. Geophys. 43 (2000) 157–165, https://doi.org/10.1016/S0926-9851(99)00055-5.

[20] L.E. Besaw, P.J. Stimac, Deep convolutional neural networks for classifying GPR Bscans, Detection and Sensing of Mines, Explosive Objects, and Obscured Targets XX, International Society for Optics and Photonics, 2015, p. 945413.

[21] P. Gader, B. Nelson, H. Frigui, G. Vaillette, J.M. Keller, Fuzzy logic detection of landmines with Ground Penetrating Radar, Signal Process. 80 (6) (2000) 1069–1084, https://doi.org/10.1016/S0165-1684(00)00020-7.

[22] P. Falorni, L. Capineri, L. Masotti, G. Pinelli, 3-D radar imaging of buried utilities by features estimation of hyperbolic diffraction patterns in radar scans, Proceedings of the Tenth International Conference on Ground Penetrating Radar, 1 2004 90-9017959-3, pp. 403–406.

[23] J. Illingworth, J. Kittler, A survey of the Hough transform, Computer Vision, Graphics, and Image Processing 44 (1) (1988) 87–116, https://doi.org/10.1016/S0734-189X(88)80033-1.

[24] C. Windsor, L. Capineri, P. Falorni, S. Matucci, G. Borgioli, The estimation of buried pipe diameters using Ground Penetrating Radar, Insight-Non-Destructive Testing and Condition Monitoring. 47 (7) (2005) 394–399, https://doi.org/10.1784/insi.2005.47.7.394.

[25] H. Zhou, M. Tian, X. Chen, Feature extraction and classification of echo signal of Ground Penetrating Radar, Wuhan University Journal of Natural Sciences. 10 (6) (2005) 1009–1012, https://doi.org/10.1007/BF02832458.

[26] R. Ghozzi, S. Lahouar, S.A. Louis, C. Souani, K. Besbes, Peak detection of GPR data with lifting wavelet transform (LWT), International Conference on Advanced Systems and Electric Technologies (IC_ASET), IEEE, 2017, pp. 34–37.

[27] C. Mass, J. Schmalzl, Using pattern recognition to automatically localize reflection hyperbolas in data from Ground Penetrating Radar, Comput. Geosci. 58 (2) (2013) 116–125, https://doi.org/10.1016/j.cageo.2013.04.012.

[28] P. Kaur, K.J. Dana, F.A. Romero, N. Gucunski, Automated GPR rebar analysis for robotic bridge deck evaluation, IEEE Transactions on Cybernetics. 46 (10) (2015) 2265–2276, https://doi.org/10.1109/TCYB.2015.2474747.

[29] P. Asadi, M. Gindy, M. Alvarez, A machine learning based approach for automatic rebar detection and quantification of deterioration in concrete bridge deck Ground Penetrating Radar B-scan images, KSCE J. Civ. Eng. 23 (2019) 2618–2627, https://doi.org/10.1007/s12205-019-2012-z.

[30] Y. LeCun, Y. Bengio, G. Hinton, Deep learning, Nature. 521 (7553) (2015) 436–444, https://doi.org/10.1038/nature14539.

[31] S. Caorsi, G. Cevini, Neural networks trained by scattered electromagnetic data for GPR applications, Proceedings of the 2nd International Workshop onAdvanced Ground Penetrating Radar, IEEE, 2003, pp. 228–233.

[32] L.E. Besaw, P.J. Stimac, Deep learning algorithms for detecting explosive hazards in Ground Penetrating Radar data, Proceedings of SPIE-The International Society for Optical Engineering 9072 (2014) 9072Y, https://doi.org/10.1117/12.2052592.

[33] W.T. Lei, F.F. Hou, J.C. Xi, Q.Y. Tan, M.D. Xu, X.Y. Jiang, G.Y. Liu, Q.Y. Gu, Automatic hyperbola detection and fitting in GPR B-scan image, Autom. Constr. 106 (2019) 102839, https://doi.org/10.1016/j.autcon.2019.102839.

[34] K. Dinh, N. Gucunski, T. Duong, An algorithm for automatic localization and detection of rebars from GPR data of concrete bridge decks, Autom. Constr. 89 (2018) 292–298, https://doi.org/10.1016/j.autcon.2018.02.017.

[35] T.H. Ling, H.R. Liu, S.W. Gong, F. Huang, Construction and application of a new biorthogonal wavelet basis for a quantitative analysis of GPR signals, J. Appl. Geophys. 170 (2019) 103837, https://doi.org/10.1016/j.jappgeo.2019.103837.

[36] P. Bordón, B. Néstor, P. Martinelli, Automatic detection of pipe-flange reflections in GPR data sections using supervised learning, J. Appl. Geophys. 170 (2019) 103856, https://doi.org/10.1016/j.jappgeo.2019.103856.

[37] A. Ristić, Ž. Bugarinović, M. Vrtunski, M. Govedarica, Point coordinates extraction from localized hyperbolic reflections in GPR data, J. Appl. Geophys. 144 (2017) 1–17, https://doi.org/10.1016/j.jappgeo.2017.06.003.

[38] L. Mertens, R. Persico, L. Matera, S. Lambot, Automated detection of reflection hyperbolas in complex GPR images with no a priori knowledge on the medium, IEEE Trans. Geosci. Remote Sens. 54 (1) (2015) 580–596, https://doi.org/10.1109/TGRS.2015.2462727.

[39] S. Zhao, I. Al-Qadi, Pavement drainage pipe condition assessment by GPR image reconstruction using FDTD modeling, Construct. Build Mater. 154 (2017) 1283–1293, https://doi.org/10.1016/j.conbuildmat.2017.06.103.

[40] J.R. Ernst, Full-waveform inversion of crosshole radar data based on 2-D finite-difference time-domain solutions of Maxwell's equations, IEEE Trans. Geosci. Remote Sens. 45 (9) (2007) 2807–2828, https://doi.org/10.1109/TGRS.2007.901048.

[41] C. Warren, A. Giannopoulos, I. Giannakis, gprMax: open source software to simulate electromagnetic wave propagation for Ground Penetrating Radar, Comput. Phys. Commun. 209 (2016) 163–170, https://doi.org/10.1016/j.cpc.2016.08.020.

[42] M. Sipos, B.G. Thompson, Electrodynamics on a grid: the finite-difference time-domain method applied to optics and cloaking, Am. J. Phys. 76 (4) (2008) 464–469, https://doi.org/10.1119/1.2835056.

[43] H. Zhao, L.J. Gelius, M. Tygel, E.H. Nilsen, A.K. Evensen, 3D prestack Fourier Mixed-Domain (FMD) depth migration for VTI media with large lateral contrasts, J. Appl. Geophys. 168 (2019) 118–127, https://doi.org/10.1016/j.jappgeo.2019.06.009.

[44] P. Whiting, Extended FK domain migration? An efficient variable velocity algorithm, Explor. Geophys. 20 (2) (1989) 281–285, https://doi.org/10.1071/EG989281.

[45] H.L. Kennedy, An Efficient Frequency-domain Velocity-filter Implementation for Dim Target Detection, 2010 International Conference on Digital Image Computing: Techniques and Applications, IEEE, 2010, pp. 39–44.

[46] H.M. Jol, Ground Penetrating Radar: Theory and Applications, 1st ed., Elsevier Science, UK, 2009, https://doi.org/10.1016/B978-0-444-53348-7.00019-3.

[47] M. Mitchell, An Introduction to Genetic Algorithms, MIT Press, Cambridge, England, 1996 (ISBN: 0-262-13316-4(HB)).

[48] A. Mccrea, R. Navon, Application of GA in optimal robot selection for bridge restoration, Autom. Constr. 13 (6) (2004) 803–819, https://doi.org/10.1016/j.autcon.2004.05.002.

[49] Y. Cheng, W.D. Yu, Q. Li, GA-based multi-level association rule mining approach for defect analysis in the construction industry, Autom. Constr. 51 (2015) 78–91, https://doi.org/10.1016/j.autcon.2014.12.016.

[50] B. Anvari, P. Angeloudis, W.Y. Ochieng, A multi-objective GA-based optimisation for holistic manufacturing, transportation and assembly of precast construction, Autom. Constr. 71 (2016) 226–241, https://doi.org/10.1016/j.autcon.2016.08.007.

[51] D.E. Goldberg, Genetic Algorithms in Search, Optimization, and Machine Learning, 1st ed., Addison-Wesley Longman Publishing Co., MA, United States, 1989https://dl.acm.org/doi/book/10.5555/534133.